ChemComm

COMMUNICATION

View Article Online
View Journal | View Issue

Cite this: *Chem. Commun.*, 2017, 53, 9277

Received 14th June 2017,
Accepted 27th July 2017

DOI: 10.1039/c7cc04609j

rsc.li/chemcomm

Aligned cobalt-based Co@CoO_x nanostructures for efficient electrocatalytic water oxidation†

Jing Qi,[a] Wei Zhang *[a] and Rui Cao *[ab]

Aligned cobalt metal nanoparticles were prepared from the pyrolysis of cobalt oxalate nanoplate precursors for efficient electrocatalytic water oxidation. The 2D morphology of the precursor guided the 2D alignment of the derived cobalt metal nanoparticles. The as-prepared Co@CoO_x electrocatalyst requires an ultra-low overpotential of 289 mV to achieve a current density of 10 mA cm^{-2} on a simple glassy carbon (GC) electrode in a 1 M KOH aqueous solution. The metallic nature of the bulk of the electrocatalyst and the compact alignment of the nanoparticles can facilitate the inner- and inter-particulate charge transfers.

In the initial steps of photosynthesis, water is oxidized into oxygen.[1] The electrons and protons released from water oxidation play important roles in the subsequent solar energy storage.[2] Artificial photosynthesis based on water splitting has attracted increasing attention in the past few decades to store the solar energy in hydrogen gases.[3] It is inevitable and significant to develop efficient catalysts for water oxidation, which is the bottleneck reaction of water splitting.[4]

CoO_x-based materials have long been investigated as efficient oxygen evolution reaction (OER) electrocatalysts.[5] To fabricate an efficient solid material-based electrocatalyst, special efforts have to be made in enhancing the electronic conductivity of the material. Thus, many Co-based non-oxide materials (nitride, selenide, sulfide and phosphide) have been reported with a strong metallic nature.[6] These materials displayed superior electrocatalytic performances due to their improved electronic conductivities, as compared with insulating or semiconductive CoO_x-based materials. Wu and co-workers reported the metallic Co_4N nanowire arrays for highly efficient OERs. They found that the surface CoO_x layer, which provided the necessary active catalytic sites, will become thicker after OER tests.[6a] Hu and co-workers investigated the surface of CoP to indicate the formation of CoO_x species during OERs.[6d] Similar surface oxidation of CoS was also observed by Zhang and co-workers for OERs.[7] All these findings indicate the probability of the surface oxidation of Co-based non-oxide materials to form the true active sites.

We propose herein to synthesize Co metal nanostructures, and subsequently, we create *in situ* CoO_x species on a metallic surface by an anodic polarization. This Co@CoO_x nanostructure is expected to efficiently electrocatalyze the OER due to the following reasons. First, the Co metal will intrinsically have a much better electronic conductivity as compared to semi-metallic Co-based nitride, selenide, sulfide and phosphide.[8] Second, CoO_x sites are formed where the charges and OH^- anions, which are also the OER substances, can reach. Thus, the *in situ* electrochemically generated surface CoO_x sites on the Co metal surface will be abundant and optimally accessible for OER substances.[9]

To create Co metals, we selected the pyrolysis of a CoC_2O_4 precursor under an inert atmosphere to prepare aligned Co metal nanoparticles. The morphology of the CoC_2O_4 precursor was regulated *via* a solvothermal reaction between $Co(OAc)_2{\cdot}4H_2O$ and diethyl oxalate in ethanol. The controlled release of $C_2O_4^{2-}$ anions from the hydrolysis of diethyl oxalate under an ethanol environment was the key determinant to prepare the CoC_2O_4 nanoplates. The 2D nanoplate morphology guided the subsequent compact alignment of the Co metal nanoparticles during pyrolysis, preserving the 2D morphology. The Co metal nanoparticles stacked closely ensuring high inter-particulate charge transfer. The as-prepared aligned metallic Co nanoparticles displayed excellent electrocatalytic OER performance in a 1 M KOH aqueous solution, affording a current density of 10 mA cm^{-2} at a low overpotential of 289 mV on a simple GC electrode. Moreover, the 2D alignment of the particles can in principle prevent the dissolution and ripening of Co metal nanoparticles, as compared with isolated nanoparticles synthesized from traditional methods.[10] The pyrolysis of oxalates to generate metallic nanostructures may be expanded for other emerging electrocatalytic applications.

The evolution of the Co-based material toward the electrocatalytic OER is illustrated in Fig. 1. Without the addition of any oxalate-containing reagent, discrete nanoprisms were formed

[a] *School of Chemistry and Chemical Engineering, Shaanxi Normal University, Xi'an 710119, China. E-mail: zw@snnu.edu.cn, ruicao@ruc.edu.cn*
[b] *Department of Chemistry, Renmin University of China, Beijing 100872, China*
† Electronic supplementary information (ESI) available. See DOI: 10.1039/c7cc04609j

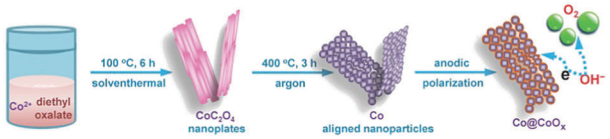

Fig. 1 The evolution of the Co-based material toward electrocatalytic OER.

under similar conditions (Fig. 2a). The hydrolysis of metal acetate hydrate in ethanol to form uniform $M(OH)_x(OAc)_y$ nanoprisms was previously reported by Lou and co-workers.[11] With the addition of sodium oxalate, nonuniform aggregates were prepared (Fig. 2b). The co-precipitation between the Co^{II} cation and the oxalate anion is not well controlled in this case. With diethyl oxalate, nanoplates with a cobalt oxalate hydrate phase were prepared (Fig. 2c). The X-ray diffraction (XRD) pattern of the sample (red line, Fig. 2l) is consistent with that of orthorhombic $CoC_2O_4{\cdot}2H_2O$ (*Cccm*, JCPDS 25-0250). From a deeper observation of the structure, the 2D nanoplates are composed of aligned nanostrips with close contacts (Fig. S1a, ESI†). The cobalt oxalate hydrate was calcined under argon gas to synthesize the expected cobalt metal nanostructures. At relatively lower temperatures (200 and 300 °C), only dehydration happened to the cobalt oxalate hydrate (eqn (S1), ESI†), as indicated in the XRD patterns of the samples (purple and green lines, Fig. 2l). The dehydrated cobalt oxalate has a crystal structure of the monoclinic CoC_2O_4 (*P*21/*n*, JCPDS 37-0719). The morphology of the material remained almost unchanged after the dehydration at 200 °C (Fig. S1b, ESI†), but the alignment of the nanostrips became more compact after the dehydration at 300 °C (Fig. S1c, ESI†). At an elevated thermal treatment temperature of 400 °C, the decomposition of the cobalt oxalate happened to form the cobalt metal (eqn (S2), ESI†). The XRD analysis (blue line, Fig. 2l) indicates the formation of a mixture of the hexagonal Co ($P6_3/mmc$, JCPDS 05-0727) and the cubic Co ($Fm\bar{3}m$, JCPDS 15-0806) metals. The hexagonal close-packed (hcp) cobalt metal has the characteristic XRD peaks at the 2θ angles of 41.7°, 44.8°, 47.6° and 76.0°, whereas the strongest diffraction peaks of the cubic close-packed (fcc) cobalt metal are at 44.2°, 51.5° and 75.9°.[12] After the phase conversion from CoC_2O_4 to Co, individual nanoparticles with a size of approximately 10–20 nm are formed (Fig. 2d–h). These Co nanoparticles aligned compactly to keep the 2D morphology, which is oriented by the 2D topology of the CoC_2O_4 nanoplate precursor. The compact density of the nanoparticles is observed to be $\sim$2900 μm^{-2}. The compact structure helps the efficient inter-particulate charge transfer and the prevention of the dissolution and ripening of particles during the OER.[13] Moreover, as observed from the TEM images (Fig. 2f–h), abundant pores are left from the packing of the Co nanoparticles. These open spaces are beneficial for mass diffusion during an electrocatalytic reaction.[13,14] The HRTEM image of the nanoparticle indicates the lattice fringes of the hcp Co (100) plane with a spacing of 0.215 nm. The high angle annular dark field (HAADF) scanning TEM (STEM) image of the aligned cobalt nanoparticles and the EDX elemental mapping images of Co and O are displayed in Fig. 2i–k, indicating the uniformity of the Co dispersion and the presence of the surface oxygen-containing adducts. At a higher thermal treatment temperature of 500 °C, the nanoparticles became discrete with a larger particle size (Fig. S1d, ESI†). The XRD analysis indicates the formation of a CoO phase in the Co metals (gray line, Fig. 2l). The formation of cobalt oxide is a side reaction (eqn (S3), ESI†) in the pyrolysis of cobalt oxalate at high temperatures.[15]

Thermogravimetric analysis was carried out to identify the weight losses of $CoC_2O_4{\cdot}2H_2O$ under an inert atmosphere (Fig. S2, ESI†). Physical characterizations of the $CoC_2O_4{\cdot}2H_2O$ before and after its conversion to the Co metal were also performed using N_2 sorption, infrared spectroscopy, Raman spectroscopy, and XPS analysis (Fig. S3–S5, ESI†). The results further confirmed the conversion from the oxalate to the metal and the surface partial oxidation of the cobalt metal after pyrolysis.

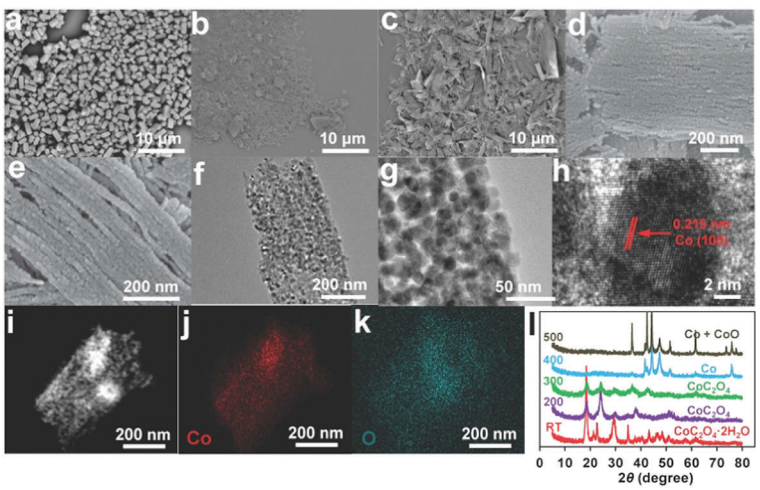

Fig. 2 The SEM images of the Co-based materials synthesized (a) without any oxalate-containing reagent, (b) with sodium oxalate and (c) with diethyl oxalate. The (d and e) SEM and (f–h) TEM images of the aligned cobalt metal nanoparticles derived from the pyrolysis of the cobalt oxalate nanoplates at 400 °C for 3 h in Ar. (i–k) The HAADF STEM image and the corresponding elemental mapping images of the cobalt nanoparticles. (l) The XRD patterns of the Co-based materials obtained from the pyrolysis of the cobalt oxalate at different temperatures.

The cobalt oxalate nanoplates and their pyrolysis-derived cobalt metal nanoparticles were studied for electrocatalytic water oxidation using linear sweep voltammetry (LSV), cyclic voltammetry (CV), controlled potential electrolysis (CPE), Tafel analysis, electrochemical impedance spectroscopy (EIS) and capacitive current analysis. The OER performances of the Co-based materials prepared at different pyrolysis temperatures are shown in Fig. S6 (ESI†). The aligned cobalt metal nanoparticles dominated in the electrocatalytic OER activity, as compared with their counterparts (Fig. S6, ESI†) and the commercial Ir/C catalyst (Fig. 3a). For the cobalt metal electrocatalyst, the overpotential (η) is merely 289 mV in a 1 M KOH aqueous solution using a simple GC electrode to drive a current density (j) of 10 mA cm^{-2}, which is a benchmark current density equivalent to a 12.3% solar-to-hydrogen efficiency for a photovoltaic device.[16] The overpotentials at current densities of 50 and 100 mA cm^{-2} are 344 and 375 mV, respectively. The turnover frequency at η = 375 mV is calculated to be 0.05 s^{-1} based on the total Co atoms on the electrode. This high performance is among the top values for OER electrocatalysts regardless of the use of electrode supports with high surface areas (carbon cloth, carbon paper, and metal foams).[5a,6c,d,7,14,17] A comparison of the OER performances between the Co@CoO$_x$ nanoparticles and some Co-based electrocatalysts in recent publications is provided in Table S1 (ESI†). In contrast, the overpotentials at j = 50 mA cm^{-2} are 373 and 401 mV for the benchmarked commercial Ir/C catalyst and the cobalt oxalate, respectively.

The cobalt metal electrocatalyst also displayed a superior stability under 24 h of electrolysis at 1.55 V *vs.* the reversible hydrogen electrode (RHE, all potentials are *vs.* RHE unless otherwise stated). The CPE currents are stabilized around 17 and 3 mA cm^{-2} without iR compensation for the cobalt metal and the cobalt oxalate, respectively (Fig. 3b). The sample is also stable after storage under dry conditions for one week, as observed from the SEM images in Fig. S7 (ESI†). The Faradaic efficiency of the OER is calculated to be close to 100% based on the theoretical and experimental amounts of evolved oxygen (Fig. S8, ESI†). The Ir/C catalysts displayed an obvious current drop during the stability test due to their poor adhesion on ITO electrodes. The cobalt metal nanoparticles retained the aligned 2D morphology after the electrolysis, as observed from the SEM image shown in Fig. S9a (ESI†). The alignment of the nanoparticles prevented dissolution and ripening, which would possibly happen to individual nanoparticles under harsh anodic polarization conditions.[10] The Raman and XPS spectra (Fig. S9, ESI†) of the post-electrolysis cobalt metals indicate the formation of surface CoO$_x$ species under anodic polarizations. The Raman peaks at 474, 607 and 669 cm^{-1} are respectively assigned to the E_g, F_{2g}, and A_{1g} vibrations of Co_3O_4, and the peak at 511 cm^{-1} is from the CoOOH species, as shown by Bell and co-worker.[18] The XPS spectrum of Co 2p also supports the above Raman results. The strong main peak of Co 2p$_{3/2}$ at 779.9 eV is very close to the values from both CoOOH and Co_3O_4.[19] The attenuated Co 2p$_{3/2}$ satellite peak, as compared with those of CoO and Co(OH)$_2$, is also observed in both CoOOH and Co_3O_4. The O 1s XPS spectrum further confirmed the OH and Co–O species on the surface of the electrocatalyst after electrolysis.[19] The surface oxide content before and after the OER test has been determined *via* a H_2 temperature programmed reduction (H_2-TPR) method, indicating the generation of stable oxide species at ~17 wt% (Fig. S10, ESI†). A cobalt oxide sample was prepared as a control study to further demonstrate the performance enhancement from the bulk conductivity (Fig. S11, ESI†).

The Tafel slope for the cobalt metal is determined to be 68.9 mV dec^{-1} from steady state currents (Fig. 3c). This value indicates that a one-electron equilibrium precedes *via* a chemical rate-limiting step in the OER.[5g] The cobalt oxalate has a higher Tafel slope of 81.1 mV dec^{-1}, suggesting a slower discharging OER process.[17a] The Nyquist plots derived from the EIS data (Fig. 3d) prove the much smaller charge transfer resistance of the cobalt metal, which is expected due to the high electronic conductivity of metals. The charging currents in the non-Faradaic

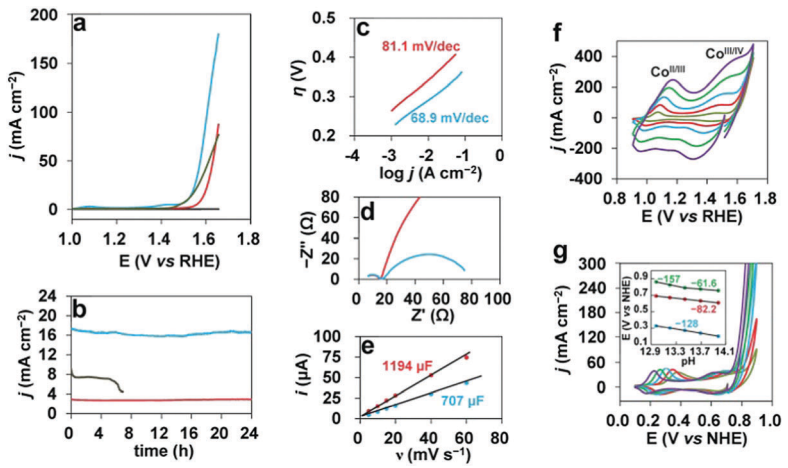

Fig. 3 (a) LSVs, (b) CPE results, (c) Tafel plots, (d) Nyquist plots and (e) charging currents of the cobalt oxalate (red) and cobalt metal (blue). The grey lines in (a) and (b) and the black line in (a) are from the commercial Ir/C and blank GC electrodes, respectively. CVs of the cobalt metal (f) at scan rates of 0.2, 0.5, 1, 2 and 3 V s^{-1} (increasing capacitive currents) in a 1 M KOH solution and (g) in 0.1, 0.2, 0.5, 1 and 2 M KOH solutions (increasing catalytic currents) at a scan rate of 0.2 V s^{-1}. The inset in (g) is the potentials (blue: $E_{1/2}$ of Co$^{II/III}$, red: $E_{1/2}$ of Co$^{III/IV}$, green: E@j = 60 mA cm^{-2}) plotted against the pH values of the electrolytes. The iR was not compensated for the CPE tests.

region (Fig. 3e and Fig. S12, ESI†) indicate the smaller electrochemical surface area from the cobalt metal (26.2 cm^2), which is consistent with its smaller BET surface area caused by the high temperature treatment (Fig. S3, ESI†). We conducted the CV studies of the cobalt metal electrocatalyst at different scan rates to get a clear picture of the pre-catalytic redox features (Fig. 3f). There are two pairs of redox peaks around 1.05 and 1.44 V before the OER event. The first redox feature is associated with the $Co^{II/III}$ couple for the formation of $Co^{III}OOH$ species, which widely exists in Co-based OER electrocatalysts under basic conditions.[5b,c,18] The second redox feature is from the $Co^{III/IV}$ couple, as identified previously from electron paramagnetic resonance studies for the formation of $Co^{IV}O_2$.[5b] The OER can only be triggered at higher potentials after the two oxidations of the cobalt catalyst. The reactions are proposed in eqn (S4)–(S6) (ESI†). The potential responses of i/ν and $i/\sqrt{\nu}$ (Fig. S13, ESI†) indicate the kinetic controls of the capacitive currents and mass diffusions, respectively.[20] The i/ν value correlates to the surface capacitance of the electrocatalyst. The linearity of $i \propto \nu$ is demonstrated by the fixed i/ν values regardless of the scan rates. The $i \propto \nu$ section covers the whole pre-catalytic region except the oxidation events (1.2–1.4 V), indicating the semiconductive nature of the surface species arisen from the oxidation of the cobalt metal. The two pre-catalytic redox features are dependent on but not proportional to the scan rates due to the mass diffusion of the hydroxide anions (*vide infra*). The $i \propto \sqrt{\nu}$ section is consistent with the previously reported Co-based porous films, suggesting that the good mass diffusion is attributed to the aligned nanostructure.[20] We also performed the CV studies of the cobalt metal in KOH solutions of different pH values (Fig. 3g). The two pre-catalytic redox peak positions can be linearly fitted to the pH values with slopes of −128 and −82.2 mV dec^{-1}, indicating the proton-coupled electron transfer (PCET) processes for the formation of Co–OH intermediates before the OER.[5g] The potentials at the OER current density of 60 mA cm^{-2} display two linear response regions to the pH values. In less concentrated KOH solutions (<0.5 M), the slope is −157 mV dec^{-1}, and this value is −61.6 mV dec^{-1} in KOH solutions of higher concentrations. Considering the Tafel slope of 68.9 mV dec^{-1} in a 1 M KOH solution, we can obtain a reaction order of 0.89 on pH based on eqn (S7) (ESI†).[21] This value suggests an inverse first-order dependence on the proton activity for the OER in a 1 M KOH solution. Thus, the OER pathway involves the nucleophilic attack by OH^- to the high-valent Co-oxo intermediates for the formation of a dioxygen bond, which is believed to be the rate-determining step in the OER.[3a]

In summary, aligned Co nanoparticles were prepared in a novel manner from the pyrolysis of cobalt oxalate nanoplates. The metal nanoparticles, intrinsically, have an efficient inner-particulate charge transfer, and they stack together to facilitate the inter-particulate charge transfer. The material electrocatalyzed water oxidation highly efficiently. The 2D alignment of the particles prevented the dissolution and ripening of Co metal nanoparticles, delivering ultra-stable water electrolysis.

We are grateful for the support from the Fundamental Research Funds for Central Universities (2017CBZ003 and GK201603037), the Starting Research Funds of Shaanxi Normal University, the National Natural Science Foundation of China (Grant No. 21101170, 21503126 and 21573139), and the ''Thousand Talents Program'' of China.

Notes and references

1 (*a*) Y. Tachibana, L. Vayssieres and J. R. Durrant, *Nat. Photonics*, 2012, **6**, 511; (*b*) S. J. A. Moniz, S. A. Shevlin, D. J. Martin, Z.-X. Guo and J. Tang, *Energy Environ. Sci.*, 2015, **8**, 731.
2 W.-J. Ong, L.-L. Tan, Y. H. Ng, S.-T. Yong and S.-P. Chai, *Chem. Rev.*, 2017, **116**, 7159.
3 (*a*) W. Zhang, W. Lai and R. Cao, *Chem. Rev.*, 2017, **117**, 3717; (*b*) Y. P. Zhu, C. Guo, Y. Zheng and S.-Z. Qiao, *Acc. Chem. Res.*, 2017, **50**, 915.
4 (*a*) B. Weng, F. Xu, C. Wang, W. Meng, C. R. Grice and Y. Yan, *Energy Environ. Sci.*, 2017, **10**, 121; (*b*) M.-S. Balogun, W. Qiu, H. Yang, W. Fan, Y. Huang, P. Fang, G. Li, H. Ji and Y. Tong, *Energy Environ. Sci.*, 2016, **9**, 3411; (*c*) S. Chen, J. Duan, J. Ran, M. Jaroniec and S. Z. Qiao, *Energy Environ. Sci.*, 2013, **6**, 3693.
5 (*a*) X. Deng and H. Tüysüz, *ACS Catal.*, 2014, **4**, 3701; (*b*) J. B. Gerken, J. G. McAlpin, J. Y. C. Chen, M. L. Rigsby, W. H. Casey, R. D. Britt and S. S. Stahl, *J. Am. Chem. Soc.*, 2011, **133**, 14431; (*c*) J. Huang, J. Chen, T. Yao, J. He, S. Jiang, Z. Sun, Q. Liu, W. Cheng, F. Hu, Y. Jiang, Z. Pan and S. Wei, *Angew. Chem., Int. Ed.*, 2015, **54**, 8722; (*d*) T. Y. Ma, S. Dai, M. Jaroniec and S. Z. Qiao, *J. Am. Chem. Soc.*, 2014, **136**, 13925; (*e*) L. Wu, Q. Li, C. H. Wu, H. Zhu, A. Mendoza-Garcia, B. Shen, J. Guo and S. Sun, *J. Am. Chem. Soc.*, 2015, **137**, 7071; (*f*) L. Xu, Q. Jiang, Z. Xiao, X. Li, J. Huo, S. Wang and L. Dai, *Angew. Chem., Int. Ed.*, 2016, **55**, 5277; (*g*) D. K. Bediako, A. M. Ullman and D. G. Nocera, in *Solar Energy for Fuels*, ed. H. Tüysüz and C. K. Chan, 2016, vol. 371, p. 173; (*h*) Y. P. Zhu, T. Y. Ma, M. Jaroniec and S. Z. Qiao, *Angew. Chem., Int. Ed.*, 2017, **56**, 1324; (*i*) T. Ling, D.-Y. Yan, Y. Jiao, H. Wang, Y. Zheng, X. Zheng, J. Mao, X.-W. Du, Z. Hu, M. Jaroniec and S.-Z. Qiao, *Nat. Commun.*, 2016, **7**, 12876.
6 (*a*) P. Chen, K. Xu, Z. Fang, Y. Tong, J. Wu, X. Lu, X. Peng, H. Ding, C. Wu and Y. Xie, *Angew. Chem., Int. Ed.*, 2015, **54**, 14710; (*b*) L. Jiao, Y.-X. Zhou and H.-L. Jiang, *Chem. Sci.*, 2016, **7**, 1690; (*c*) T. Liu, Y. Liang, Q. Liu, X. Sun, Y. He and A. M. Asiri, *Electrochem. Commun.*, 2015, **60**, 92; (*d*) P. Wang, F. Song, R. Amal, Y. H. Ng and X. Hu, *ChemSusChem*, 2016, **9**, 472; (*e*) Y. Zhang, B. Ouyang, J. Xu, G. Jia, S. Chen, R. S. Rawat and H. J. Fan, *Angew. Chem., Int. Ed.*, 2016, **55**, 8670; (*f*) Y. Zheng, Y. Jiao, Y. Zhu, Q. Cai, A. Vasileff, L. H. Li, Y. Han, Y. Chen and S.-Z. Qiao, *J. Am. Chem. Soc.*, 2017, **139**, 3336; (*g*) B. Bayatsarmadi, Y. Zheng, Y. Tang, M. Jaroniec and S.-Z. Qiao, *Small*, 2016, **12**, 3703.
7 J. Wang, H.-X. Zhong, Z.-L. Wang, F.-L. Meng and X.-B. Zhang, *ACS Nano*, 2016, **10**, 2342.
8 J.-X. Feng, H. Xu, Y.-T. Dong, S.-H. Ye, Y.-X. Tong and G.-R. Li, *Angew. Chem., Int. Ed.*, 2016, **55**, 3694.
9 D. Guo, J. Qi, W. Zhang and R. Cao, *ChemSusChem*, 2017, **10**, 394.
10 L. Ruan, E. Zhu, Y. Chen, Z. Lin, X. Huang, X. Duan and Y. Huang, *Angew. Chem., Int. Ed.*, 2013, **52**, 12577.
11 L. Yu, B. Guan, W. Xiao and X. W. Lou, *Adv. Energy Mater.*, 2015, **5**, 1500981.
12 Y. Deng, X. Xiong, J. P. Zou, L. Deng and M. J. Tu, *J. Alloys Compd.*, 2015, **618**, 497.
13 L. Liao, S. Wang, J. Xiao, X. Bian, Y. Zhang, M. D. Scanlon, X. Hu, Y. Tang, B. Liu and H. H. Girault, *Energy Environ. Sci.*, 2014, **7**, 387.
14 J. Qi, W. Zhang, R. Xiang, K. Liu, H.-Y. Wang, M. Chen, Y. Han and R. Cao, *Adv. Sci.*, 2015, **2**, 1500199.
15 D. M. Zhilin and R. M. Peetz, *J. Chem. Educ.*, 2014, **91**, 119.
16 J. S. Luo, J. H. Im, M. T. Mayer, M. Schreier, M. K. Nazeeruddin, N. G. Park, S. D. Tilley, H. J. Fan and M. Grätzel, *Science*, 2014, **345**, 1593.
17 (*a*) C. C. L. McCrory, S. Jung, J. C. Peters and T. F. Jaramillo, *J. Am. Chem. Soc.*, 2013, **135**, 16977; (*b*) J. Wang, H.-X. Zhong, Y.-L. Qin and X.-B. Zhang, *Angew. Chem., Int. Ed.*, 2013, **52**, 5248.
18 B. S. Yeo and A. T. Bell, *J. Am. Chem. Soc.*, 2011, **133**, 5587.
19 J. Yang, H. Liu, W. N. Martens and R. L. Frost, *J. Phys. Chem. C*, 2010, **114**, 111.
20 C. Costentin, T. R. Porter and J.-M. Savéant, *J. Am. Chem. Soc.*, 2016, **138**, 5615.
21 Y. Surendranath, M. W. Kanan and D. G. Nocera, *J. Am. Chem. Soc.*, 2010, **132**, 16501.

